Two-dimensional modeling of polymer wet spinning: The effects of mass transfer dynamics on structural properties

Hasan Zerze, Anthony J. McHugh

Department of Chemical and Biomolecular Engineering, Lehigh University, Bethlehem, Pennsylvania
Correspondence to: A. J. McHugh (E-mail: ajm8@lehigh.edu)

ABSTRACT: In this work, a two-dimensional model of polymer wet spinning that couples simultaneous momentum and energy transport with ternary diffusion and phase separation processes is presented and its predictions for a model system are discussed. The uniqueness of the model lies in its two-phase nature and ability to predict important characteristics of the wet spinning process, such as the locking-in of axial velocity, mass transfer behavior, and internal structure formation along the spinline. The model predicts growth of the two-phase gel that forms and the porous fractions within it, along with the compositions of the polymer-rich and solvent-nonsolvent-rich phases. The appearance of a skin-core structure that depends on the system and operating conditions is also predicted. These features are demonstrated through analyses of the isothermal wet spinning of poly(acrylonitrile) solutions in dimethlysulfoxide using two different nonsolvent coagulants, water and ethanol. © 2014 Wiley Periodicals, Inc. J. Appl. Polym. Sci. **2015**, *132*, 41772.

INTRODUCTION

Wet spinning is a widely applied industrial process used in fiber manufacturing. In this process, a polymer solution is extruded through a perforated plate into a coagulation bath having a nonsolvent mixture, and the precipitated polymer threads are bundled at the end of the spinline by a rotating wheel.

A great deal of experimental work has been done to elicit fruitful information on the phase equilibrium thermodynamics of many of the ternary systems used in the wet-spinning process. In addition, wet-spun fibers have extensively been characterized to relate their mechanical and structural properties to the process conditions, such as temperature, bath composition, stretch ratio,[1,2] and the type of the nonsolvent.[3] However, except for a limited number of measurements, such as velocity and force, on-line analyses of these systems have been limited, due in part to the microscopic length-scales characteristic of the radial dimensions, and the difficulty of making *in situ* measurements in the bath environment. In consequence, modeling studies[4] can be a useful adjunct to gain insights on the key variables controlling the process.

Ziabicki (1976) has reviewed the earlier studies on wet-spinning process in detail.[5] More recently, Oh *et al.* (1996) investigated the HNO_3 composition within poly(acrylonitrile) (PAN) fibers as a function of bath length, and reported satisfactory agreement of their experimental data with the model results.[4] They

found the coefficients of an empirical expression to relate the diffusion coefficient to the solvent concentration. Chen *et al.* (2006) modeled the wet spinning of PAN in dimethlysulfoxide (DMSO)–water solution as an unsteady-state diffusion process in one direction.[6] Kalabin and Pakshver (1997) employed a two-dimensional (2D) theoretical model to predict the gel layer thickness along the spinline.[7] They introduced two distinct diffusive regions to account for the effect of gelation on the diffusion rate.

A detailed literature survey indicates that previous studies have focused on pseudo two-component and single-phase modeling of the wet spinning. Since most of the important properties of wet spun fibers can be related to their two-phase structure, we consider it very important to incorporate the ternary phase separation dynamics in the modeling.

The purpose of this article is to demonstrate a 2D theoretical model of the wet-spinning process that incorporates the ternary thermodynamics, along with an associated parameter for the two-phase fiber structure that develops along the spinline. Our model is capable of predicting the relative proportions of the polymer-rich and solvent-nonsolvent-rich phases, as well as the compositions within both, as functions of the radial and the axial positions. Results will be shown to compare favorably with experimental observations. The wet-spinning system chosen for modeling is PAN in DMSO and two different nonsolvents, water, and ethanol.
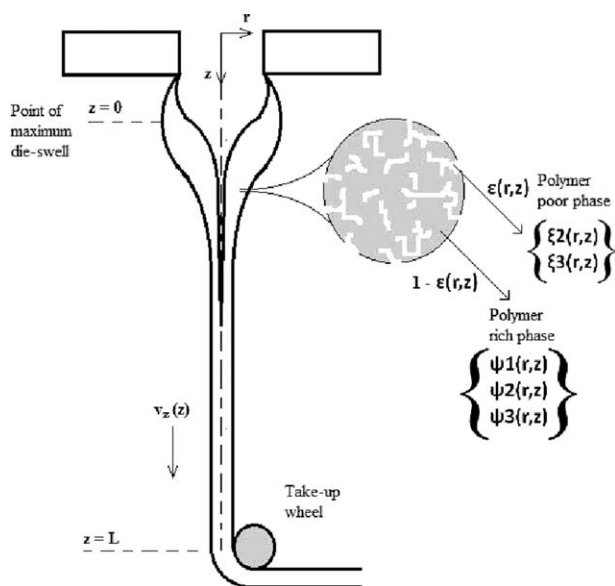
Figure 1. Schematic description of the wet spinning system. The symbols are defined in the text.

METHODOLOGY AND MODEL CONSTRUCTION

System Definition and Summary of the Assumptions

Figure 1 illustrates the wet-spinning system modeled in this study. As seen, immediately on emerging from the spinneret, polymer solution contacts with a nonsolvent solution in the bath and separates into a polymer-rich phase and a polymer-poor phase while being drawn in the axial direction. The main assumptions of our model are as follows:

1. The system is 2D and at steady state.
2. Fiber cross section is circular.
3. The system is isothermal.
4. Fiber is drawn with a uniaxial extension.
5. Mixtures within the fiber and the bath are both ideal.
6. Polymer diffusion into the bath is neglected.
7. The off-diagonal terms in the ternary diffusion equations are neglected.
8. Radial solvent and nonsolvent diffusion rates are expressed by Fickian equations, for each of the two phases. Axial mass transfer is assumed to be dominated by bulk convection, while the radial mass transfer has both diffusive and convective contributions.
9. Two-phase compositions achieve instant equilibrium everywhere within the fiber.
10. Nonsolvent volume fraction on the binodal curve for the polymer rich phase is constant. This assumption is supported by the parallelism of binodal with the polymer–solvent axis for most of the ternary systems.
11. Polymer volume fraction in the polymer poor phase is zero at all points.
12. At the point of maximum die-swell, the fiber has a uniform composition across the radius.

Flow Kinematics

Uniaxial extensional flow kinematics are assumed and the contribution of diffusive mass transfer in all the components of the velocity gradient tensor is neglected.[8]

$$\underline{\nabla}\ \underline{v} = \begin{bmatrix} \dfrac{dv_z}{dz} & 0 & 0 \\ 0 & \dfrac{\partial v_r}{\partial r} & 0 \\ 0 & 0 & \dfrac{v_r}{r} \end{bmatrix} = \begin{bmatrix} \dfrac{dv_z}{dz} & 0 & 0 \\ 0 & -\dfrac{1}{2}\dfrac{dv_z}{dz} & 0 \\ 0 & 0 & -\dfrac{1}{2}\dfrac{dv_z}{dz} \end{bmatrix} \quad (1)$$

In eq. (1), v_z and v_r are velocity components in the axial and radial directions, respectively. The radial velocity component can be expressed in terms of the axial velocity gradient:

$$v_r = -\frac{r}{2}\frac{dv_z}{dz} \quad (2)$$

Transport Equations

Continuity Equation. Integration of the equation of continuity for the polymer, assuming no polymer transport to the bath solution, gives the following equation for the fiber radius, R:

$$R = \left(\frac{W_1}{\rho_{1o}\bar{\phi}_1\pi v_z}\right)^{1/2} \quad (3)$$

In eq. (3), W_1, ρ_{1o} and $\bar{\phi}_1$ are the mass flow rate of the polymer, pure polymer density and the radially averaged volume fraction of the polymer, respectively. The differential form of this equation can be expressed as follows (see Appendix A.1 for derivation):

$$\frac{dR}{dz} = -\frac{R}{2v_z}\frac{dv_z}{dz} - \frac{k_{y2}}{v_z\rho_{2o}}\left(\rho_{2,\mathrm{film}} - \rho_{2,\mathrm{bath}}\right) - \frac{k_{y3}}{v_z\rho_{3o}}\left(\rho_{3,\mathrm{film}} - \rho_{3,\mathrm{bath}}\right) \quad (4)$$

In eq. (4), the k_{yi} are mass transfer coefficients for the solvent and nonsolvent transfer to or from the bath, and the ρ_i are the associated bath-side interfacial (subscript film) and bulk bath (subscript bath) compositions.

Momentum Equation. Neglecting the inertial force due to solvent and nonsolvent transport, the radially averaged momentum equation for a steady state and uniaxial extensional flow becomes the following:[8]

$$\bar{\rho}R^2 v_z\frac{\partial v_z}{\partial z} = \frac{\partial}{\partial z}\left[R^2(\bar{\tau}_{zz} - \bar{\tau}_{rr})\right] + 2R\tau_{rz}^a\big|_R + s\frac{\partial R}{\partial z} + R^2\bar{\rho}g \quad (5)$$

In eq. (5), $\bar{\rho}$ is the cross-sectional averaged density, $\bar{\tau}_{zz}$ and $\bar{\tau}_{rr}$ are the cross-sectional averaged normal components of the stress tensor in the axial and radial directions, respectively, s is the surface tension of the filament, and g is the gravitational constant. The shear stress due to surface friction, $\tau_{rz}^a\big|_R$, is expressed as:

$$\tau_{rz}^a\big|_R = -\frac{1}{2}f\rho_{\mathrm{film}}v_z^2 \quad (6)$$

where f and ρ_{film} are the friction coefficient and density of the film layer, respectively.

Mass Transfer Equation. A 2D mass transfer model is adopted. The continuity equations for solvent and nonsolvent are the following (see Appendix for derivation):

$$\frac{\partial\rho_2}{\partial z} = \frac{1}{v_z}\left[-v_r\frac{\partial\rho_2}{\partial r} - \frac{1}{r}\left\{\frac{\partial(rj_2)}{\partial r} + \frac{\rho_2}{\rho_{1o}}\frac{\partial}{\partial r}\left[r(K_2j_2 + K_3j_3)\right]\right\}\right] \quad (7)$$

and

$$\frac{\partial \rho_3}{\partial z}=\frac{1}{v_z}\left[-v_r\frac{\partial \rho_3}{\partial r}-\frac{1}{r}\left\{\frac{\partial(rj_3)}{\partial r}+\frac{\rho_3}{\rho_{1o}}\frac{\partial}{\partial r}\left[r(K_2j_2+K_3j_3)\right]\right\}\right] \quad (8)$$

where ρ_i values are the mass concentrations of the solvent ($i = 2$) and the nonsolvent ($i = 3$). $K_i = 1 - \rho_{1o}/\rho_{io}$, and j_i denotes the radial diffusive flux of species i.

Constitutive Equations

Given the relatively low take-up speeds characteristic of wet spinning (i.e., low Deborah number), Newtonian behavior can be assumed. Thus, the stress-deformation rate behavior will be given by:

$$\overrightarrow{\overrightarrow{\tau}}=\mu\left[\overrightarrow{\nabla}\overrightarrow{v}+\left(\overrightarrow{\nabla}\overrightarrow{v}\right)^T\right]=2\mu\,\overrightarrow{\nabla}\overrightarrow{v} \quad (9)$$

In the solution region ($\varepsilon = 0$) within the fiber, viscosity is assumed to be described by:

$$\eta=\eta_{PR}(T,\psi_1,\psi_2) \quad (10)$$

In the gel region, on the other hand, the viscosity is assumed to be a linear combination of the two-phase compositions:

$$\eta(T,\varepsilon,\psi_1,\psi_2,\xi_2)=\varepsilon\,\eta_{PP}(T,\xi_2)+(1-\varepsilon)\,\eta_{PR}(T,\psi_1,\psi_2) \quad (11)$$

In these equations, ε is the wet porosity which represents the fraction of the polymer-free phase at a point within the gel region. Subscripts PP and PR denote the polymer-free and polymer-rich phases, respectively, and ξ_i and ψ_i are the compositions of species i in the polymer-free and polymer-rich phases, respectively. A protocol to determine ε, ξ_i, and ψ_i is prescribed as follows: Given φ_i, the single phase representation for the composition, the compositions in the two phases, ξ_i and ψ_i are calculated by solving the following equations for each component:

$$\left\{\begin{array}{l}\varepsilon=0,\text{if }\phi_3<\phi_{3cr}\\\psi_3=\phi_{3cr},\text{if }\phi_3\geq\phi_{3cr}\end{array}\right\} \quad (12)$$

$$\phi_i=\varepsilon\xi_i+(1-\varepsilon)\,\psi_i \quad (13)$$

$$a_i(\psi_1,\psi_2)=a_i(\xi_2) \quad (14)$$

Activities, a_i, of solvent and nonsolvent are calculated using the following expressions from Flory–Huggins theory:[9]

$$a_2=\phi_2\exp\left[1-\phi_2-\phi_3\frac{\overline{V_2}}{V_3}-\phi_1\frac{\overline{V_2}}{V_1}+\left(\phi_3 g_{32}\frac{\overline{V_2}}{V_3}+\phi_1 g_{21}\right)\right.$$
$$\left.\times(\phi_3+\phi_1)-\phi_3\phi_1 g_{31}\frac{\overline{V_2}}{V_3}+h_3 h_2\phi_3\frac{dg_{32}}{dh_2}\frac{\overline{V_2}}{V_3}-\phi_2\phi_1^2\frac{dg_{21}}{d\phi_1}\right] \quad (15)$$

$$a_3=\phi_3\exp\left[1-\phi_3-\phi_2\frac{\overline{V_3}}{V_2}-\phi_1\frac{\overline{V_3}}{V_1}+(\phi_2 g_{32}+\phi_1 g_{31})(\phi_2+\phi_1)\right.$$
$$\left.-\phi_2\phi_1 g_{21}\frac{\overline{V_3}}{V_2}-h_3 h_2\phi_2\frac{dg_{32}}{dh_2}-\phi_2\phi_1^2\frac{dg_{21}}{d\phi_1}\frac{\overline{V_3}}{V_2}\right] \quad (16)$$

where $h_2 = \phi_2/(\phi_2 + \phi_3)$ and $h_3 = \phi_3/(\phi_2 + \phi_3)$. Concentration-dependent interaction parameters (g_{ij}) are given in the literature.[3] $\overline{V}_i$ is the molar volume of pure component i. The diffusive mass flux of species i within the fiber is expressed in terms of the volume-weighted average of the fluxes from the polymer-rich and polymer-free phases, respectively:

$$j_i=\varepsilon j_{i,PP}+(1-\varepsilon)j_{i,PR} \quad (17)$$

$$j_i=-\varepsilon\rho_{PP}D_{i,PP}\frac{\partial w_{i,PP}}{\partial r}-(1-\varepsilon)\rho_{PR}D_{i,PR}\frac{\partial w_{i,PR}}{\partial r} \quad (18)$$

In these equations, w_i and D_i are the mass fraction and the diffusion coefficient of species i, respectively.

Boundary Conditions

The following conditions hold at the point of maximum die swell and at the take-up wheel:

$$\phi_i|_{z=0}=\phi_{id} \quad (19)$$

$$v_z|_{z=0}=v_{zo} \quad (20)$$

$$v_z|_{z=L}=v_L \quad (21)$$

At the fiber center:

$$\left.\frac{\partial\phi_i}{\partial r}\right|_{r=0}=0 \quad (22)$$

At the fiber surface, a convective mass transfer boundary condition holds if the concentration difference between the bath and the film side is significant. When the film composition is close to the bath composition, we adopt a constant surface composition boundary condition. Thus:

If $|\phi_{2,film}-\phi_{2,bath}|>0.05$

$$j_i|_{r=R}=k_y(\rho_{i,film}-\rho_{i,bath}) \quad (23)$$

otherwise,

$$\left.\frac{\partial\phi_i}{\partial z}\right|_{r=R}=0 \quad (24)$$

Finally, composition of the polymer-free phase at the surface is assumed to be identical to that of the film solution:

$$\xi_i|_{r=R}=\phi_{i,film} \quad (25)$$

Material Properties

The glass transition temperature of the polymer mixture, T_g is calculated using the following relation:[10]

$$T_g=\frac{T_{g1}+(KT_{g23}-T_{g1})\phi_{23}}{1+(K-1)\phi_{23}} \quad (26)$$

where $\phi_{23}=\phi_2+\phi_3$ and $T_{g23}=(\phi_2\,T_{g2}+\phi_3\,T_{g3})/(\phi_2+\phi_3)$. For the system in this study, it is assumed that $K = 2.5$.

The zero-shear viscosity of the polymeric mixture is calculated by the use of the following set of equations:[11,12]

$$A=\frac{E_n}{2.3\,R\,T} \quad (27)$$

$$\mu_1=A\left(\frac{T_g}{T}-1\right) \quad (28)$$

$$\mu_2=33.3\frac{T_g}{T}-27.8 \quad (29)$$

$$\mu_3=\frac{8(T_g/T)-6.5-0.01A}{0.6-0.02A} \quad (30)$$

$$\mu=\log(10^{\mu_1}+10^{\mu_2}+10^{\mu_3}) \quad (31)$$

Table I. Physical Properties of Components in the Modeled System

Properties	PAN	DMSO	Water	Ethanol
ρ_{io} (kg/m^3)	1200	1100	998	789
T_g (K)	360[15]	153	182	106
k [W/(m.K)]	0.2[16]	See text	See text	See text
C_P [j/(kg.K)]	1260	See text	4187	4187
M_i (kg/mol)	78.0	0.07813	0.018015	0.04607
T_{cr} (K)	–	720.0	647.3	514
T_b (K)	–	462	373.2	351.5
$\overline{\omega}$	–	0.2094	0.344	0.635
$E_{a,\mu}$ (j/mol)	–	14,260	16,137	13,909
A_μ (Pa.s)	–	6.288×10^{-6}	1.357×10^{-6}	3.802×10^{-6}
$E_{a,diff}$ (j/mol)	–	14,900	17,550	17,550
A_{diff} (m^2/s)	–	2.998×10^{-7}	2.761×10^{-6}	1.727×10^{-6}

$$\log\eta^*(T) = E_n\left(\frac{0.052 - 8.5\times10^{-5}T_g}{T_g}\right) - 1.4 + \mu + 3.4\log\left(\frac{M_1}{M_{1cr}}\right) \tag{32}$$

$$\log\eta(T,\phi) = \log\eta^*(T) + 5\ \log\phi_1 \tag{33}$$

We used $E_n = 44{,}000$ j/mol and $M_{1cr} = 1.3$ kg/mol for PAN. Zero-shear viscosity for a polymer-free mixture is calculated by the use of a commonly known viscosity blending number, VBN:[13]

$$VBN_i = 14.534\ \ln(\ln(v_i + 0.8)) + 10.975 \tag{34}$$

$$VBN_{mix} = w_2 VBN_2 + w_3 VBN_3 \tag{35}$$

$$v_{mix} = \exp\left(\exp\left(\frac{VBN_{mix} - 10.975}{14.534}\right)\right) - 0.8 \tag{36}$$

In these expressions, v is kinematic viscosity in centistokes. Pure substance viscosities of solvent and nonsolvent are calculated from an Arrhenius-type expression:

$$\mu = A_\mu \exp\left(\frac{E_{a,\mu}}{RT}\right) \tag{37}$$

where A_μ and $E_{a,\mu}$ are viscosity coefficient and activation energy for viscosity, respectively (see Table I). The binary diffusion constant $D_{i,PP}$ in the polymer-free solution is estimated using the volume-weighted logarithmic average of the self diffusivities of the corresponding pure substances:

$$\log D_{i,PP} = \phi_2 \log D_{22}^{self} + \phi_3 \log D_{33}^{self} \tag{38}$$

Self-diffusivities were estimated by the following Arrhenius expression:

$$D_{ii}^{self} = A_{diff} \exp\left(-\frac{E_{a,diff}}{RT}\right) \tag{39}$$

where A_{diff} and $E_{a,diff}$ are the multiplication constant and the activation energy for diffusivity, respectively (see Table I).

For the binary solutions in the bath and film, thermal conductivity, k was calculated using a mixing rule:

$$k = \phi_2^2 k_2 + 2\phi_2\phi_3 k_{23} + \phi_3^2 k_3 \tag{40}$$

$$k_{23} = \frac{2}{k_2^{-1} + k_3^{-1}} \tag{41}$$

Pure substance conductivities of solvent and nonsolvent are calculated using the equation below:

$$k_{i,i=2,3} = \frac{\left(1.11/M_i^{1/2}\right)\left(3 + 20(1 - T_r)^{2/3}\right)}{3 + 20(1 - T_{br})^{2/3}} \tag{42}$$

where $T_r = T/T_{cr}$ and $T_{br} = T_b/T_{cr}$. For the ternary solution within the fiber, thermal conductivity is calculated similarly by applying the mixing rule twice. Mixture heat capacity is estimated using mass fraction weighting:

$$C_P = w_1 C_{P1} + w_2 C_{P2} + w_3 C_{P3} \tag{43}$$

C_{P1} and C_{P3} values are listed in Table I, for PAN and water. For DMSO, the following expression is used:[14]

$$C_{P2}[\text{j/(kg.K)}] \doteq \frac{1}{M_2}$$
$$\left[C_{P2o} + R\left(1.586 + \frac{0.490}{1 - T_{r2}} + \overline{\omega_2}\left(4.2775 + 6.3\frac{(1 - T_{r2})^{1/3}}{T_{r2}} + \frac{0.4355}{1 - T_{r2}}\right)\right)\right] \tag{44}$$

In this equation, $\overline{\omega_2}$ is the accentric factor of DMSO (see Table I) and the ideal gas heat capacity for DMSO is expressed as below:

$$C_{P2o} = 6.94 + 5.6\ \times10^{-2}\ T - 2.27\times10^{-5}\ T^2 \tag{45}$$

Heat and Mass Transfer Coefficients and Friction Coefficient

The Nusselt number, Nu and the heat transfer coefficient, h are obtained using a correlation for pure parallel flow:[17]

$$\text{Nu} = \frac{hD}{k_{film}} = 0.420\ Re_D^{1/3} \tag{46}$$

In eq. (46), D is the fiber diameter and the Reynolds number, Re_D is calculated as follows:

$$Re_D = \frac{v_z \rho_{film} D}{\mu_{film}} \tag{47}$$

Table II. Conditions of the Modeled Wet Spinning Process

Process parameters	Values
Mass flow rate at die exit, W_d (kg/s)	3.52×10^{-7}
Volume fraction of DMSO in the dope, ϕ_{2d}	0.77
Volume fraction of nonsolvent in the dope, ϕ_{3d}	0.01
System temperature, T (K)	313
Die swell ratio, dsr	1.67
Dope diameter, D_d (m)	1.5×10^{-4}
Take-up velocity, v_L (m/s)	0.02
Length of spinline, L_o (m)	0.1
Volume fraction of DMSO in the bath, ϕ_{2bath}	0.70
Volume fraction of nonsolvent in the bath, ϕ_{3bath}	0.30

Figure 2. Effect of bath composition on the axial velocity profile along the spinline. The other operating conditions are listed in Table II. [Color figure can be viewed in the online issue, which is available at wileyonlinelibrary.com.]

Having obtained the Nusselt number, the Sherwood number is calculated using the Chilton–Colburn analogy:

$$Sh \ (Sc)^{-1/3} = Nu \ (Pr)^{-1/3} \tag{48}$$

where the Schmidt and Prandtl numbers are $Sc = \mu/(\rho D_i)$ and $Pr = (\mu C_P)/k$, respectively. Mass transfer coefficient, k_y is calculated using the definition of the Sherwood number:

$$Sh = \frac{k_y D}{D_i} \tag{49}$$

The friction coefficient is calculated according to the equation below:[18]

$$f = 0.68 \ Re_D^{-0.80} \tag{50}$$

Coordinate Transformation and Nondimensionalization
The moving boundary in the radial dimension is fixed via normalization of the radial coordinate by the fiber radius, $R(z)$:

$$r^* = \frac{r}{R(z)} = \frac{r}{R_o R^*(z)} \tag{51}$$

where $R^*(z) = R(z)/R_o$. The other nondimensional variables are defined as below:

$$z^* = \frac{z}{L}; \quad \vec{v}^* = \frac{\vec{v}}{v_{zo}}; \quad j_i^* = \frac{j_i}{\rho_o v_{zo}};$$
$$\bar{\rho}^* = \frac{\bar{\rho}}{\bar{\rho}_o}; \quad s^* = \frac{s}{s_o}; \quad \vec{\tau}^* = \vec{\tau}\left(\frac{L}{\eta_o v_{zo}}\right) \tag{52}$$

Differentials take the following forms:

$$\left.\frac{\partial}{\partial z}\right|_r = \frac{1}{L}\left.\frac{\partial}{\partial z^*}\right|_{r^*} - \frac{r^*}{LR^*}\frac{dR^*}{dz^*}\left.\frac{\partial}{\partial r^*}\right|_{z^*}; \quad \frac{d}{dz} = \frac{1}{L}\frac{d}{dz^*};$$
$$\left.\frac{\partial}{\partial r}\right|_z = \frac{1}{R_o R^*}\left.\frac{\partial}{\partial r^*}\right|_{z^*}; \quad \left.\frac{\partial^2}{\partial r^2}\right|_z = \frac{1}{R_o^2 R^{*2}}\left.\frac{\partial^2}{\partial r^{*2}}\right|_{z^*} \tag{53}$$

Numerical Method
The differential equations were discretized in both the axial and radial directions. Twenty nodes with smaller spacing near the surface were used in the radial direction. Discretized equations were solved simultaneously along the axial coordinate u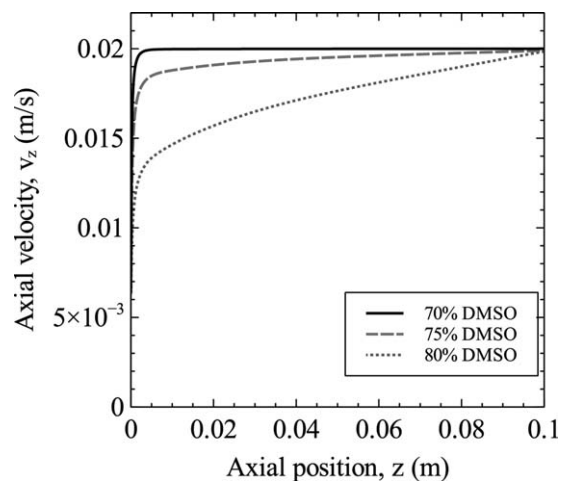sing a fourth-order Runge–Kutta method in combination with a shooting method. At the point of maximum die-swell ($z = 0$), the initial conditions were assigned as introduced in the previous section. The calculation procedure is as follows:

First, an initial guess for $(dv_z^*/dz^*)|_{z=0}$ is assigned to forward the step in the z-direction with a step-size of $\Delta z = 10^{-5}$. At each value of z, the nondimensionalized continuity, momentum and mass transfer equations are used in the given order to update the values of the axial derivatives. A fourth-order Runge–Kutta algorithm is also employed to refine approximate values of the axial derivatives. The calculated velocity at the spinline exit is compared with the predefined value of take-up speed v_L and a new guess for $(dv_z^*/dz^*)|_{z=0}$ is assigned accordingly to reinitiate an updated set of iterations. This procedure is repeated until the take-up speed is estimated with an acceptable error value.

RESULTS AND DISCUSSION

Flow Characteristics
To illustrate model predictions for the flow characteristics of wet spinning, axial velocity profiles are presented for different bath compositions in Figure 2. As seen, axial velocity increases along the spinline and asymptotically approaches the take-up velocity. Han and Segal (1970) reported a similar trend in their experimental and modeling results.[19] These results indicate a so-called locking-in behavior similar to that predicted and seen in other spinning processes.[8,20] On the contrary, the model of Kalabin and Pakshver exhibited a parabolic-like increase in the axial velocity.[7]

Our predictions suggest that the axial velocity profile is strongly affected by the bath composition. As the solvent fraction in the bath decreases, the velocity is seen to approach the take-up speed sooner. The apparent extensional viscosity profiles shown in Figure 3 exhibit orders of magnitude increases along the spinline and show a similar locking-in behavior, suggesting that the flow kinematics are affected by the bath composition primarily through the effect on the viscosity. In our model,
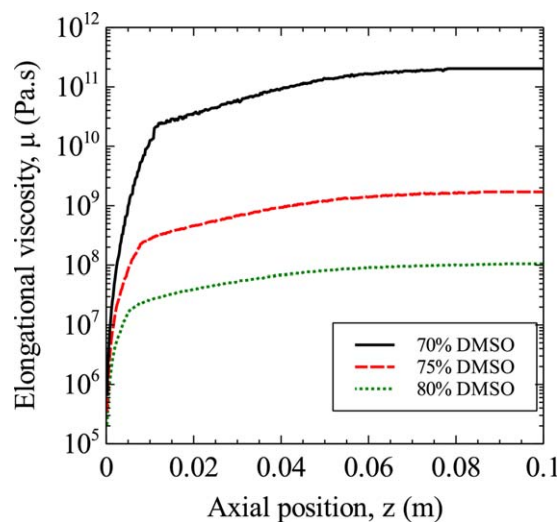
Figure 3. Effect of bath composition on the viscosity profile along the spinline. The other operating conditions are listed in Table II. [Color figure can be viewed in the online issue, which is available at wileyonlinelibrary.com.]

Figure 5. Effect of draw ratio on the tensile force at the take-up. The other operating conditions are listed in Table II.

viscosity is directly related to the phase separation [see eq. (11)]. Particularly, the viscosity depends dominantly on the composition within the polymer-rich phase. In their study, Han and Segal (1970) expressed their measured extensional viscosity as a second-order polynomial function of solvent fraction and argued that the coagulation due to mass and heat transfer mainly influenced the elongational viscosity.[19] The predictions in our case are a consequence of a combination of more rapid phase separation and higher polymer fractions within the polymer-rich phase with increased nonsolvent in the bath.

Tensile forces at take-up for different bath compositions shown in Figure 4, indicate that higher force is predicted for lower solvent fraction in the bath solution. The reason for this can be attributed to both more rapid mass transfer, inducing earlier
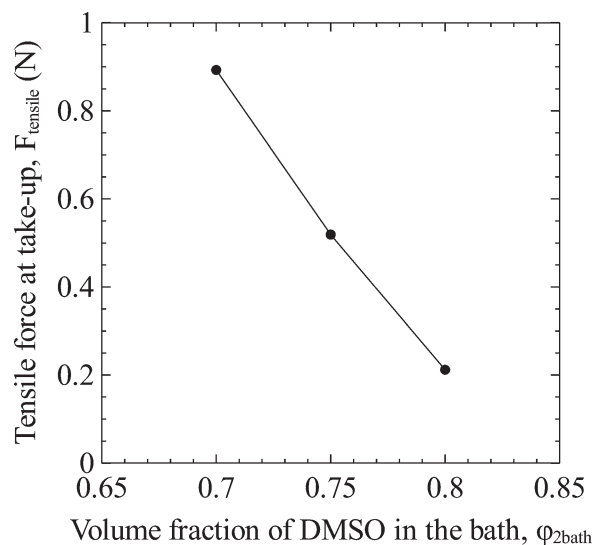
solidification, and an eventually higher polymer fraction within the polymer-rich phase. This result is in agreement with the predicted viscosity curves for different bath compositions (see Figure 3). Han and Segal (1970) argued that spinning under high tensile force (or stress) is a significant factor which may improve the mechanical properties of the finished threads by increasing molecular orientation during the processing.[19]

The effect of draw ratio on the tensile force at take-up is illustrated in Figure 5. The curves exhibit a concave-downward increase with draw ratio, similar to experimental results found by Han and Segal.[19,21]

Mass Transfer Dynamics and Fiber Quality

Model predictions of radial solvent composition profiles for the PAN–DMSO–water system are shown in Figure 6. In the first half of the spinline ($z^* < 0.5$), solvent fraction is predicted to decrease in both the radial and axial directions, reflecting the effect of the radial outward flux of solvent in this region of the spinline. However, as shown, the solvent composition remains essentially constant along the second half of the spinline ($0.5 < z^* < 1.0$), despite the presence of a radial concentration gradient. This is further illustrated in Figure 7. Figure 7(a) on the left shows solvent composition profiles just below the spinneret ($z^* = 0.02$). At this point, the fiber cross-section consists of two regions: a single phase solution ($0 < r^* < 0.7$) separated by a two-phase gel region ($0.7 < r^* < 1.0$) which grows inward away from the point of fiber-bath contact. The associated ternary composition path shown on the phase diagram (right) illustrates that compositions in the polymer-rich (ψ_i) and solvent-nonsolvent rich (ξ_i) regions of the gel lie along the respective ends of the equilibrium tie lines. As further precipitation (i.e., gelation) occurs along the spin line, these compositions move deeper into the binodal region. Figure 7(b) illustrates the profiles at the end of the spinline. By this point, the gel has grown across the entire radius (see also Figure 6) and the profiles for the overall (ϕ_2) and two-phase (ψ_i, ξ_i)

Figure 4. Effect of bath composition on tensile force calculated at the take-up. The other operating conditions are listed in Table II.
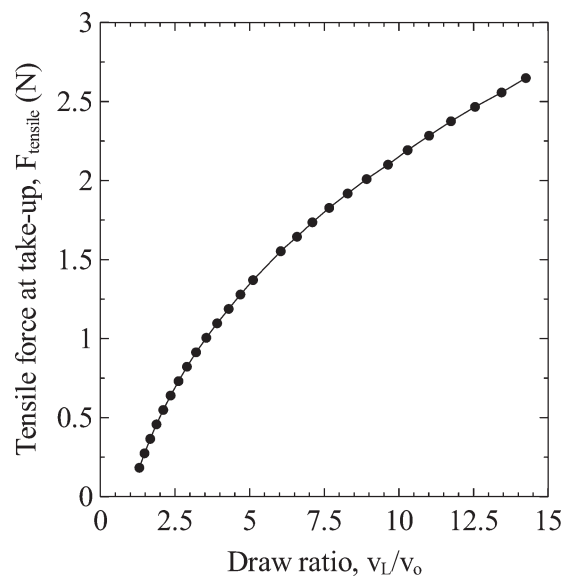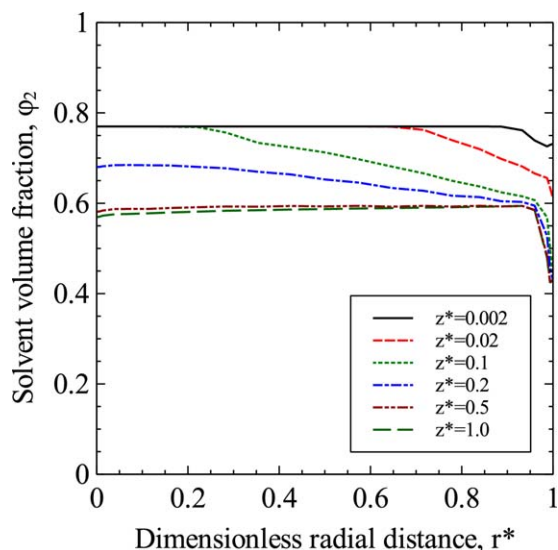
Figure 6. Prediction of solvent composition profiles at various axial positions along the spinline. The operating conditions are listed in Table II. [Color figure can be viewed in the online issue, which is available at wileyonlinelibrary.com.]

compositions exhibit the locking-in feature described earlier. It is important to note that though the equilibrium phase compositions remain constant across the entire radius and are fixed at the two ends of a tie line, the single phase composition (ϕ_2) still exhibits a locked-in radial profile as a consequence of the nonuniform wet-porosity profiles (See, e.g., Figure 8). However,

since all radial compositions lie along the same equilibrium tie line [Figure 7(b)], the diffusive fluxes are zero. To our knowledge, these results are unique to this study, and may be attributed to the separate calculation of the diffusive fluxes through the two-phase structure.

Predictions of the effects of bath composition and dope composition on the radial distribution of fiber porosity, suggest formation of a denser (less porous) skin layer surrounding a core with higher porosity (see Figures 8 and 9). This is in good agreement with the experimental results on the morphology of PAN fibers reported earlier.[2,3,6] Zhang et al. (2011) examined wet-spun PAN fibers by SEM imaging and confirmed for the PAN–DMSO–water system that the radial fiber structure consists of a dense, thin-skin layer having no visible pores in combination with an intermediate dense layer having a small number of pores and a wide core domain with a loose structure.[3] Chen et al. (2006) reported dense skin thicknesses on the order of 20% of the pore radius for PAN fibers.[6] Such morphological features are also consistent with the appearance of skinned, porous structures typical of quenched phase inversion membranes.[22] Skin-core structure formation is an important feature of wet spinning whose control is needed to enhance fiber mechanical properties. In consequence, we have further investigated the effects of wet-spinning conditions on predictions of the structure formation.

Results for porosity profiles at different bath compositions are presented in Figure 8. These demonstrate that porosity becomes more uniform across the fiber radius, and decreases in the inner
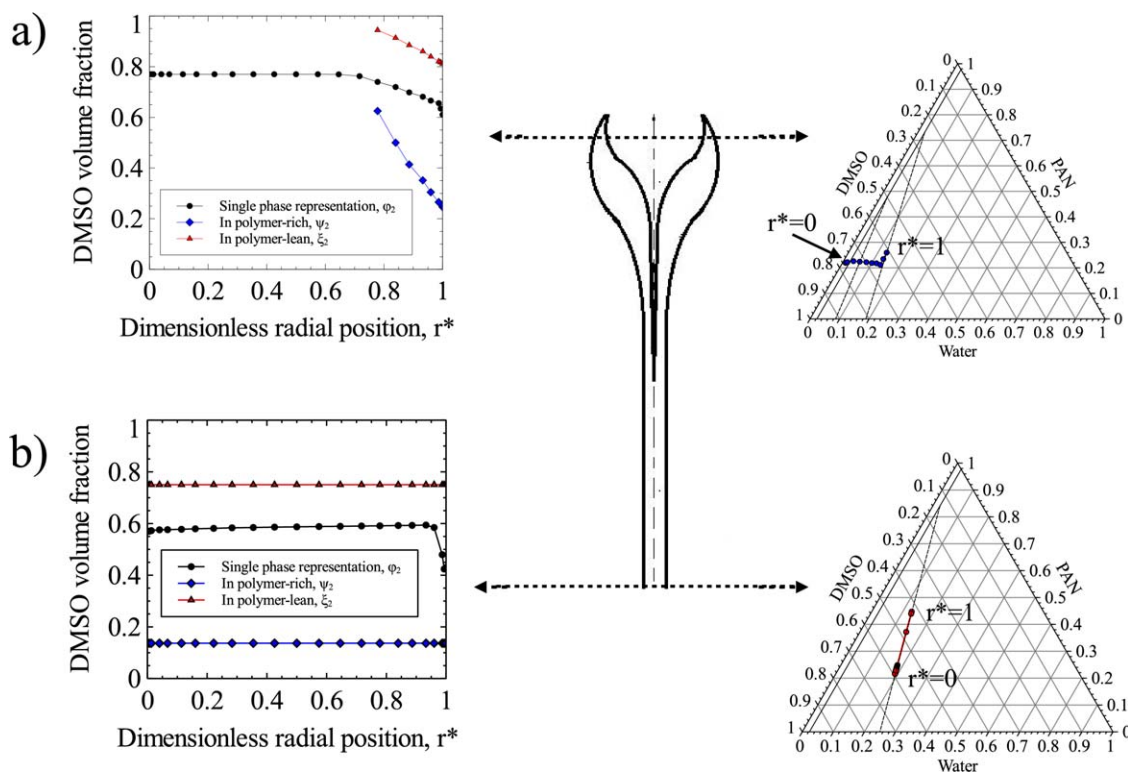

Figure 7. Solvent radial profiles (left) and associated ternary composition paths (right) for two axial locations [(a) $z^* = 0.02$, (b) $z^* = 1$] along the spinline. Dashed lines on phase diagrams denote equilibrium tie lines (see text for discussion). [Color figure can be viewed in the online issue, which is available at wileyonlinelibrary.com.]
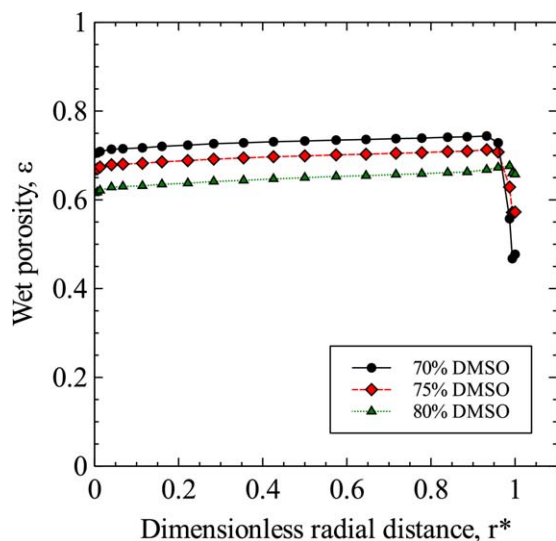
Figure 8. Radial wet porosity profiles within the exiting fiber ($z^* = 1$) for various bath compositions. The other operating conditions are listed in Table II. [Color figure can be viewed in the online issue, which is available at wileyonlinelibrary.com.]

core, as solvent concentration in the bath is increased. Zhang et al. (2011) argued that rapid solidification at the fiber surface due to the precipitating strength of the bath leads to the formation of a skin layer that also slows the subsequent diffusion of solvent from the fiber.[3] On the other hand, our results show that solvent diffusion is completed during the spin process, leading to more uniform, radial compositions in both phases prior to take-up. Hence, our predictions of increasing porosity with a decrease in solvent composition in the bath suggest the controlling feature of phase equilibrium. In addition, the polymer-rich phase shrinks more when solvent extraction is favored by lowering the solvent composition in the bath (see
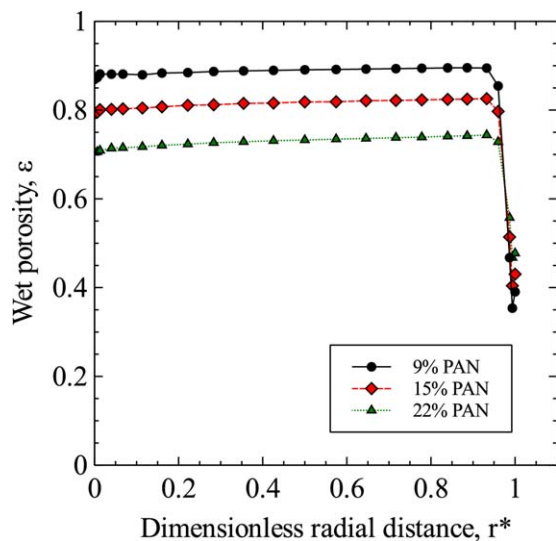
Table III. Effect of Bath Composition on the Final Polymer Fraction inside the Polymer-Rich Phase.

ϕ_{2bath}	0.70	0.75	0.80
ψ_{1f}	0.84	0.75	0.65

Table III). These results suggest that selection and control of bath composition are of particular importance in obtaining spun fiber quality.

Predicted radial porosity profiles for different polymer dope compositions are illustrated in Figure 9. With increasing polymer fraction in the dope, porosity profile levels in the interior of the fiber are seen to decrease. Also, once phase equilibrium is attained throughout the fiber and the mass transfer is completed, compositions in the polymer-free phase become nearly identical to those in the bath. This is confirmed by our model predictions of polymer-free phase composition profiles and is consistent with observations described in Ziabicki.[5] Similarly, polymer fractions within the dense phase also equilibrate prior to the take-up for the runs at constant bath conditions. Thus, changes in the dope composition affect the relative proportions of the two phases rather than exerting an influence on the eventual compositions within the separate phases. These observations explain the observed proportionality between the dope composition and the fraction of the polymer-rich phase obtained at the end of the process.

Although the porosity profile depends strongly on both the bath composition and the polymer fraction in the dope, skin-layer thickness is not affected significantly. In all cases studied for the PAN–DMSO–water system, skin thickness is found to be on the order of one-tenth of the fiber radius.

Effect of Nonsolvent Type on the Model Predictions
Predictions have also been made for a wet-spinning system composed of PAN–DMSO–ethanol. Axial composition profiles

Figure 9. Radial wet porosity profiles in the exiting fiber ($z^* = 1$) for various polymer compositions in the dope solution. The other operating conditions are listed in Table II. [Color figure can be viewed in the online issue, which is available at wileyonlinelibrary.com.]
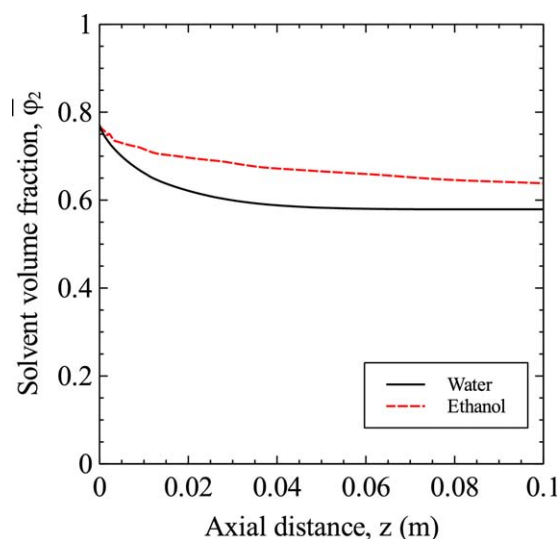

Figure 10. Effect of nonsolvent type on the axial solvent composition profile. The operating conditions are listed in Table II. [Color figure can be viewed in the online issue, which is available at wileyonlinelibrary.com.]
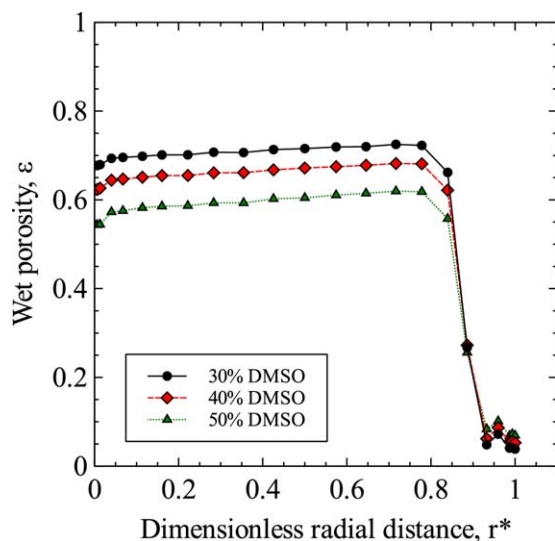
Figure 11. Wet porosity profiles in the exiting fiber ($z^* = 1$) for different bath compositions (nonsolvent is ethanol). The other operating conditions are listed in Table II. [Color figure can be viewed in the online issue, which is available at wileyonlinelibrary.com.]

of DMSO are illustrated in Figure 10 for the two different non-solvents—water and ethanol. Both curves exhibit an asymptotic decrease in solvent concentration along the spinline, typical of behaviors seen experimentally.[4] However, as shown in Figure 10, the decrease in solvent composition is more rapid for the case of nonsolvent water. We believe this reflects the higher precipitating power of water in combination with the larger miscibility gap between the dope composition and the binodal curve for the PAN–DMSO–ethanol system.[3]

In order to compare the influence of the nonsolvents on the wet-spinning performances, results for fiber porosity profiles obtained for the PAN–DMSO–ethanol system are shown in Figure 11. The profiles for different bath compositions exhibit a common layered structure with a very dense thin skin surrounding a wide and loose portion, similar to those predicted for the PAN–DMSO–water system. However, skin thicknesses in this case are on the order of 20% of the total radius, which is about twice that suggested for the PAN–DMSO–water system. In addition, as seen in Figure 11, porosity in the core decreases with increasing solvent concentration in the bath. On the other hand, in the example of fibers generated in a 40% ethanol bath reported by Zhang et al., the morphology exhibited a uniformly dense structure across the radius.[3]

CONCLUSIONS

A 2D, two-phase model has been constructed to investigate the mass transfer and structure formation dynamics during the wet-spinning process. The commonly observed skin-formation phenomenon is successfully predicted for PAN fibers. The nonsolvent type and composition of the coagulation bath have significant effects on the porosity profiles and associated composition profiles. In addition, the velocity profiles exhibit a locking-in behavior, typical of the behavior seen experimentally. Although PAN–DMSO–water and PAN–DMSO–ethanol systems

are studied in this work, the presented model is also adaptable to other wet-spinning systems.

APPENDIX

Equation for the Rate of Change of Fiber Radius Along the Spinline

Balance for species i gives:

$$-\frac{d}{dz}\left(R^2 v_z \overline{\phi_i} \rho_{io}\right) = 2Rk_{yi}\left(\rho_{i,\text{film}} - \rho_{i,\text{bath}}\right) \quad (A1.1)$$

$$-R^2 \frac{d}{dz}\left(v_z \overline{\phi_i}\right) - 2Rv_z \overline{\phi_i}\frac{dR}{dz} = \frac{2Rk_{yi}}{\rho_{io}}\left(\rho_{i,\text{film}} - \rho_{i,\text{bath}}\right) \quad (A1.2)$$

$$-R\left[v_z \frac{d\overline{\phi_i}}{dz} + \overline{\phi_i}\frac{dv_z}{dz}\right] - 2v_z \overline{\phi_i}\frac{dR}{dz} = \frac{2k_{yi}}{\rho_{io}}\left(\rho_{i,\text{film}} - \rho_{i,\text{ bath}}\right) \quad (A1.3)$$

Summing up this equation for all three species gives:

$$\frac{dR}{dz} = -\frac{R}{2v_z}\frac{dv_z}{dz} - \frac{k_{y2}}{v_z \rho_{2o}}\left(\rho_{2,\text{film}} - \rho_{2,\text{bath}}\right) - \frac{k_{y3}}{v_z \rho_{3o}}\left(\rho_{3,\text{film}} - \rho_{3,\text{bath}}\right)$$

$$(A1.4)$$

Mass Transport Equations

Assuming the mixture is ideal,

$$\rho = \rho_{1o} + K_2 \rho_2 + K_3 \rho_3 \quad (A2.1)$$

where $K_2 = 1 - \rho_{1o}/\rho_{2o}$ and $K_3 = 1 - \rho_{1o}/\rho_{3o}$.
The continuity equation gives:

$$\frac{1}{r}\frac{\partial}{\partial r}\left(r\rho v_r\right) + \frac{\partial(\rho v_z)}{\partial z} = 0 \quad (A2.2)$$

Inserting eq. (A2.1), we find:

$$\frac{1}{r}\frac{\partial}{\partial r}\left(rv_r\right) + \frac{\partial v_z}{\partial z} = -\frac{K_2}{\rho}\left[v_r \frac{\partial\rho_2}{\partial r} + v_z \frac{\partial\rho_2}{\partial z}\right] - \frac{K_3}{\rho}\left[v_r \frac{\partial\rho_3}{\partial r} + v_z \frac{\partial\rho_3}{\partial z}\right]$$

$$(A2.3)$$

The point-wise mass transfer equation for the solvent is:

$$\frac{1}{r}\frac{\partial}{\partial r}\left(r\rho_2 v_r\right) + \frac{\partial}{\partial z}\left(\rho_2 v_z\right) = -\frac{1}{r}\frac{\partial}{\partial r}\left(rj_2\right) \quad (A2.4)$$

$$\left[v_r \frac{\partial\rho_2}{\partial r} + v_z \frac{\partial\rho_2}{\partial z}\right] = -\rho_2\left[\frac{1}{r}\frac{\partial(rv_r)}{\partial r} + \frac{\partial v_z}{\partial z}\right] - \frac{1}{r}\frac{\partial(rj_2)}{\partial r} \quad (A2.5)$$

And for the nonsolvent, similarly:

$$\left[v_r \frac{\partial\rho_3}{\partial r} + v_z \frac{\partial\rho_3}{\partial z}\right] = -\rho_3\left[\frac{1}{r}\frac{\partial(rv_r)}{\partial r} + \frac{\partial v_z}{\partial z}\right] - \frac{1}{r}\frac{\partial(rj_3)}{\partial r} \quad (A2.6)$$

Combination of eqs. (A2.1, A2.3, A2.5, and A2.6) gives:

$$\frac{1}{r}\frac{\partial}{\partial r}\left(rv_r\right) + \frac{\partial v_z}{\partial z} = \frac{1}{r}\frac{1}{\rho_{1o}}\frac{\partial}{\partial r}\left[r\left(K_2 j_2 + K_3 j_3\right)\right] \quad (A2.7)$$

Further combination of eq. (A2.7) with the eqs. (A2.5 and A2.6), respectively, gives:

$$\frac{\partial\rho_2}{\partial z} = \frac{1}{v_z}\left[-v_r \frac{\partial\rho_2}{\partial r} - \frac{1}{r}\left\{\frac{\partial(rj_2)}{\partial r} + \frac{\rho_2}{\rho_{1o}}\frac{\partial}{\partial r}\left[r\left(K_2 j_2 + K_3 j_3\right)\right]\right\}\right]$$

$$(A2.8)$$

and

$$\frac{\partial \rho_3}{\partial z} = \frac{1}{v_z}\left[-v_r \frac{\partial \rho_3}{\partial r} - \frac{1}{r}\left\{\frac{\partial(rj_3)}{\partial r} + \frac{\rho_3}{\rho_{1o}}\frac{\partial}{\partial r}\left[r(K_2 j_2 + K_3 j_3)\right]\right\}\right]$$

(A2.9)

REFERENCES

1. Zeng, X.; Hu, J.; Zhao, J.; Zhang, Y.; Pan, D. *J. Appl. Polym. Sci.* **2007**, *106*, 2267.

2. Dong, X.-G.; Wang, C.-G.; Bai, Y.-J.; Cao, W.-W. *J. Appl. Polym. Sci.* **2007**, *105*, 1221.

3. Zhang, J.; Zhang, Y.; Zhao, J. *J. Polym. Bull.* **2011**, *67*, 1073.

4. Oh, S. C.; Wang, Y. S.; Yeo, Y.-K. *Ind. Eng. Chem. Res.* **1996**, *35*, 4796.

5. Ziabicki, A. Fundamentals of Fibre Formation; Wiley: New York, **1976**.

6. Chen, J.; Wang, C.-G.; Dong, X.-G.; Liu, H.-Z. *J. Polym. Res.* **2006**, *13*, 515.

7. Kalabin, A. L.; Pakshver, E. A. *Theor. Fndns. Chem. Eng.* **1997**, *31*, 520.

8. Gou, Z.; McHugh, A. J. *J. Non-Newtonian Fluid Mech.* **2004**, *118*, 121.

9. Gou, Z. Modeling of Dry Spinning of Polymer Fibers. Ph.D. Thesis, University of Illinois at Urbana-Champaign, Urbana, Illinois, **2003**.

10. Kelley, F. N.; Bueche, F. *J. Polym. Sci.* **1961**, *50*, 549.

11. Krevelen, D. W. V. Properties of Polymers: Their Estimation and Correlation with Chemical Structure; Elsevier: Amsterdam, **1990**.

12. Krevelen, D. W. V. Properties of Polymers: Their Correlation with Chemical Structure; Their Numerical Estimation and Prediction from Additive Group Contributions, 3rd ed.; Elsevier Science B.V.: Amsterdam, **1997**.

13. Maples, R. E. Petroleum Refinery Process Economics, 2nd ed.; Pennwell Books: Tulsa, OK, **2000**.

14. Reid, R. C.; Prausnitz, J. M.; Sherwood, T. K. The Properties of Gases and Liquids; McGraw-Hill: New York, **1977**.

15. Howard, W. H. *J. Appl. Polym. Sci.* **1961**, *5*, 303.

16. David, D. J.; Misra, A. Relating Materials Properties to Structure; Technomic Publishing Company: **1999**.

17. Kase, S.; Matsuo, T. *J. Appl. Polym. Sci.* **1967**, *11*, 251.

18. Sano, Y. *Dry. Technol.* **2001**, *19*, 1335.

19. Han, C. D.; Segal, L. *J. Appl. Polym. Sci.* **1970**, *14*, 2999.

20. Doufas, A. K.; McHugh, A. J.; Miller, C. *J. Non-Newton. Fluid Mech.* **2000**, *92*, 27.

21. Han, C. D.; Segal, L. *J. Appl. Polym. Sci.* **1970**, *14*, 2973.

22. Mulder, M. Basic Principles of Membrane Technology; Kluwer Academic Publishers, 2nd ed., **2000**.